Check for updates

Controls and evidence for assigning europium emission in Eu-treated CsPbCl₃ nanocrystals

Yanfei Wang, Martin Vacha 🆔 and Shun Omagari 🆔 *

Lanthanide doping of semiconductor nanocrystals is widely pursued to enhance luminescence *via* photosensitization, and lead halide perovskite nanocrystals have been frequently reported as effective hosts due to their large absorption cross sections. Here we synthesized cubic-CsPbCl₃ nanocrystals in the presence of Eu^{3+} precursors, which have been reported to exhibit strong photosensitized Eu^{3+} emission, and reproduce the emission motifs reported for Eu-treated CsPbCl₃ nanocrystals. Using centrifugation fractionation together with control experiments and spectral comparisons, we find that the ensemble Eu^{3+} line emission is dominated by Eu–ligand complex byproducts that persist through standard processing. Transmission electron microscopy confirms the presence of cubic CsPbCl₃ nanocrystals, and spot energy-dispersive X-ray spectroscopy detects Eu on individual cubic particles. Single-particle spectroscopy further reveals dilute emissive particles exhibiting anticorrelated host emission and an anomalous broad band, which we assign to a lanthanide-centered charge-transfer state (CTS), indicating a competing pathway that disfavors Eu^{3+} f–f emission from the perovskite host. Overall, these results decouple evidence for Eu-containing CsPbCl₃ nanocrystals from the origin of ensemble Eu^{3+} line emission, motivate purification and identification protocols, and demonstrate the utility of single-particle spectroscopy for assessing lanthanide-doped semiconductor nanocrystals.

1. Introduction

Trivalent lanthanide (Ln^{3+}) ions are known for their high monochromaticity and long emission lifetimes and have been used in lighting, displays, lasers, and bioimaging.[1–4] A disadvantage of Ln^{3+} ions is their small absorption cross-section, which is 3–4 orders of magnitude lower than that of typical organic phosphors, leading to low emission intensity even at unity quantum yield. One strategy to obtain intense luminescence from Ln^{3+} ions is photosensitization, in which an electronic state with a large absorption cross-section acts as an antenna and transfers energy to the emitting states of the Ln^{3+} ion. For example, Ce^{3+}, Eu^{3+}, and Tb^{3+} ions are used in fluorescent lamps, where 4f–5d, ligand-to-metal charge transfer, and $Ce^{3+} \rightarrow Tb^{3+}$ energy transfer, respectively, serve as antennae that absorb light from the UV discharge lamp.[5–7] In Ln^{3+} complexes, excited states of organic ligands play the role of antennae and transfer energy to the Ln^{3+} ion mainly *via* the triplet excited state of the ligands.[8]

A similar approach has been applied to inorganic semiconductor nanoparticles.[9] The first report of Ln^{3+}-doped inorganic semiconductor nanoparticles with photosensitized emission dates back to 2006, when Eu was incorporated into CdS

quantum dots.[10] Other host materials soon followed, including II–VI semiconductors (*e.g.*, CdSe,[11,12] ZnS[13,14]), perovskites (*e.g.*, CsPbCl₃,[15–17] CsPbBr₃[15,18–20]), and others (*e.g.*, CaZnOS,[21] In₂O₃,[22] and SnO₂[23]). In these materials, the host semiconductor is proposed to absorb light and transfer energy to Ln^{3+} ions through electron and/or energy transfer with proper host design, leading in some cases to intense Ln^{3+} luminescence.[24–26]

There was a controversy regarding whether, and how, Ln^{3+} ions were actually doped into cesium lead halide nanocrystals[18–20,26–30] until the report by Liu *et al.* in 2023.[31] Using HAADF-STEM and EDS imaging of a single ∼20 nm CsPbCl₃ nanoparticle, they unambiguously proved that Yb^{3+} ions were successfully doped, mainly by occupying lattice interstitial sites and substituting Pb^{2+} cations. Atom-probe tomography of a sub-micron CsPbCl₃ single crystal showed homogeneous doping at ∼5 at%. The finding represents a major milestone for single-particle detection of Ln^{3+}-doped nanocrystals. The low absorption cross-section (low absorption rate) combined with millisecond-scale emission lifetimes (low emission rate) of Ln^{3+} ions means a low excitation–emission cycle rate per unit time, so single-particle detection of Ln^{3+}-doped nanocrystals has traditionally required 10^3–10^5 W cm^{-2} excitation—far above the ∼10–10^2 W cm^{-2} typically used for single-molecule spectroscopy.[32–34] Although photosensitization addresses the low absorption rate, the low emission rate cannot be compensated beyond a threshold where the excitation rate exceeds the emission rate (as in Ln^{3+} complexes).

School of Materials and Chemical Technology, Institute of Science Tokyo, 2-12-1 Ookayama, Meguro, Tokyo, 152-8552, Japan. E-mail: omagari.s.aa@m.titech.ac.jp; Tel: +81 5 5734 3643

This journal is © the Owner Societies 2026

Phys. Chem. Chem. Phys., 2026, **28**, 7191–7200 | 7191

In nanocrystals, however, a few hundred Ln^{3+} ions confined in a small volume can yield higher total emission per unit time. For example, a 10 nm $CsPbCl_3$ nanocrystal doped at 5 at% contains ~ 280 Ln^{3+} ions. If each Ln^{3+} has an intrinsic 20% quantum yield in the $CsPbCl_3$ host, reliable single-particle detection is achievable in a standard setup (~ 50 W cm^{-2} excitation, 10% detection efficiency) with host $\rightarrow$ Ln^{3+} energy-transfer efficiency as low as $\sim 6\%$. For comparison, a typical organic fluorophore with $\sim 90\%$ quantum yield reaches a similar photon output under the same conditions.

The next potential ambiguity to resolve for Ln^{3+}-doped $CsPbCl_3$ nanocrystals is how Ln^{3+} emission is observed from these systems. For instance, prior reports on $CsPbCl_3$:Eu^{3+} nanocrystals from different groups clearly show the characteristic Eu^{3+} luminescence peaks, with a main peak at 612 nm,[15,18,35–38] but the emission is usually accompanied by radiative excitonic recombination of the $CsPbCl_3$ host (~ 410 nm) and/or an anomalous broad band in between, implying at least three types of emitting centers. The combinations and relative intensities of these emissions vary across reports. In many reports, the Eu^{3+} line emission is implicitly assigned to host-sensitized Eu^{3+} dopants under the assumption that the measured ensemble is a sufficiently purified population of $CsPbCl_3$:Eu^{3+} nanocrystals, an assumption often supported mainly by TEM/STEM-EDS evidence for Eu in nanocrystals. However, without purification steps that explicitly exclude Eu-containing byproducts, the sources of the emission remain ambiguous at the ensemble level; the Eu^{3+} ions that are doped in the $CsPbCl_3$ nanocrystal host may be dark, while impurities containing Eu^{3+} could actually be the source of the Eu^{3+} emission. In systems like $CsPbCl_3$ nanocrystals where the synthesized products are purified through centrifugation, there is no guarantee of full purification. Common identification techniques such as TEM (and STEM-EDS), XRD, solid-state NMR, or IR can miss impurities if they are insensitive to the measurement method. Single-particle spectroscopy is a possible workaround to address this ambiguity since they spatially separate impurities even at very low concentration.

Herein, we revisit the origin of the Eu^{3+} line-emission (and other accompanied emission) motifs commonly observed in Eu-treated $CsPbCl_3$ nanocrystal syntheses, with the specific goal of separating evidence for Eu-containing perovskite nanocrystals from evidence for the emitting Eu^{3+} species. Our approach combines centrifugation-based fractionation with control syntheses and comparative optical spectroscopy to track how Eu^{3+} emission features partition across the products of synthesis and processing. In parallel, we employ electron microscopy and spot energy-dispersive X-ray spectroscopy to confirm the presence of cubic $CsPbCl_3$ nanocrystals and to evaluate whether Eu is detectable on individual particles. Finally, we use single-particle spectroscopy to probe dilute, localized emitters that can be obscured in ensemble measurements. Together, these measurements enable a more direct assignment of Eu^{3+} emission in Eu-treated perovskite nanocrystal preparations and clarify what additional evidence is required to connect Eu^{3+} line emission to the nanocrystal host.

2. Experimental section

2.1 Materials

Cs_2CO_3 (99.9%), $PbCl_2$ (99.999%), $Eu(NO_3)_3 \cdot 6H_2O$ ($> 99.95\%$), oleic acid (OA), oleyl amine (OAm), and PMMA ($M_w \sim 350\,000$) were purchased from Sigma-Aldrich Japan. 1-Octadecene (ODE) was purchased from Tokyo Chemical Industries. Toluene was purchased from Kanto Chemical Co., Inc. All reagents were used without further purification.

2.2 Apparatus

2.2.1 Transmission electron microscopy (TEM). TEM, scanning TEM, and energy dispersive X-ray spectroscopy (EDS) measurement was done using JEOL EM-2010F (acceleration voltage 200 kV). The beam diameter was 2–5 nm for TEM and 0.5–2.4 nm for STEM/EDS measurements.

2.2.2 Macroscopic spectroscopy. UV-Vis absorption spectra were measured with a JASCO V760 spectrophotometer. Emission spectra were measured with a home-built optical fiber spectroscopy system consisting of Ocean Insight MAYA2000 Pro CCD spectrometer (spectral resolution ~ 0.66 nm) and an LED excitation source (LSM-L365A, 369 nm actual) with LDC-1C LED controller.

2.2.3 Single-particle spectroscopy. Single-particle spectroscopy was performed using a wide-field fluorescence microscope (Fig. S1). The excitation source was a 360 nm DPSS laser (UV-FN-360-100 mW-5%-LED, Changchun New Industries Optoelectronics Technology Co., Ltd). The objective was a semi-apochromatic Olympus UPlanFLN100XO2 ($\times 100$ magnification, NA 1.30). A 370 nm dichroic mirror and a 380 nm long-pass filter were used to reflect the excitation laser and isolate the emission. The excitation laser was focused onto the back focal plane of the objective, allowing wide-field illumination of the sample, which was imaged with an EMCCD camera (Andor iXon DU897).

2.3 Synthesis

The nanocrystals were synthesized using the hot injection method, as previously reported.[37] The selection of this particular report was based on how reliably and consistently the properties can be reproduced. The detailed procedure is as described below (Scheme 1).

2.3.1 Synthesis of Cs–oleate complex. Cs_2CO_3 (0.5 mmol, 0.16 g), octadecene (ODE, 6 mL), and oleic acid (OA, 0.5 mL) were added to a 100 mL 3-neck flask (Flask A). The mixture was heated to 120 °C and held for 1 hour under nitrogen atmosphere until complete dissolution of cesium carbonate. The mixture was then raised to 150 °C for 10 minutes before injection.

2.3.2 Synthesis of $CsPbCl_3$ nanocrystals. $PbCl_2$ (0.376 mmol, 0.105 g), ODE (10 mL), OA (1.4 mL), and oleylamine (OAm, 1.4 mL) were added to a 100 mL three-neck flask (Flask B). The mixture was heated to 120 °C under nitrogen for 1 hour until complete dissolution of $PbCl_2$. Next, the temperature was raised to 180 °C and maintained for 60 seconds, followed by the rapid injection of Cs–oleate solution (0.8 mL) from Flask A into Flask B. After 60 seconds, the crude solution was immediately cooled in an ice-water bath until the product solidified. Finally, the flask containing the product was removed from the bath and held at room temperature.

7192 | *Phys. Chem. Chem. Phys.*, 2026, **28**, 7191–7200

This journal is © the Owner Societies 2026
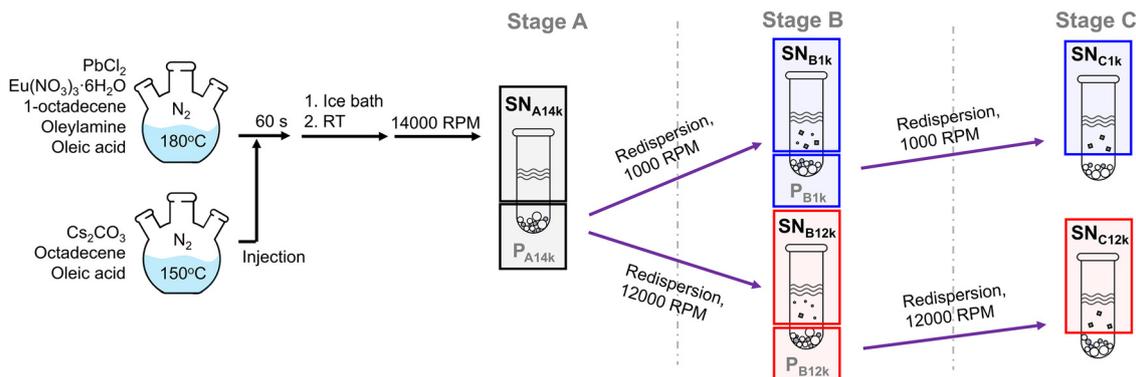
Scheme 1 Synthetic and purification scheme of $CsPbCl_3:Eu^{3+}$ nanocrystals. Stage a: supernatant after first centrifugation; stage b: supernatant of the redispersed precipitates of stage a; stage c: supernatant of the redispersed precipitates of stage b.

2.3.3 Synthesis of $CsPbCl_3:Eu^{3+}$ nanocrystals. $Eu(NO_3)_3 \cdot 6H_2O$ (0.188 mmol, 0.084 g), ODE (10 mL), OA (1.4 mL), and OAm (1.4 mL) were added to a 100 mL three-neck flask (Flask C). The mixture was heated to 120 °C under the nitrogen atmosphere for 1 hour until complete dissolution of $Eu(NO_3)_3 \cdot 6H_2O$. Then, $PbCl_2$ powder (0.188 mmol, 0.052 g) was added to the flask and heated for another 30 min. After the complete dissolution of $PbCl_2$, the temperature was increased to 200 °C for 60 seconds, followed by the rapid injection of Cs-oleate solution (0.8 mL) from Flask A to Flask C. After 60 seconds, the crude solution was immediately cooled by the ice-water bath until the product solidified. Finally, the flask containing the product was removed from the bath and held at room temperature.

2.3.4 Post-synthetic treatments. The crude products were isolated into 1.5 mL aliquots and centrifuged at 14 000 RPM (16 500 RCF) for 5 minutes. The precipitate was redispersed in 0.5 mL toluene, sonicated, and separated into two 0.25 mL portions for further centrifugation. One portion was centrifuged at 1000 RPM (80 RCF), and the other at 12 000 RPM (11 700 RCF). Each of these precipitates was redispersed in 0.5 mL toluene and sonicated. Both redispersed precipitates were then centrifuged at the same speeds as in the previous step, and their supernatants were collected. The samples were stored in dark and measured on the next day of the synthesis to minimize potential degradation and exposures to atmosphere. All samples were diluted by tenfold before the measurements.

2.3.5 Sample nomenclature. We denote supernatants as SN and precipitate as P. The letter (A, B, C) indicates the centrifugation stage; the numeric suffix gives the speed (reported as RPM). Stages B and C are obtained after redispersing the previous precipitate.

2.3.6 SN_{A14k}. Supernatant of the crude dispersion after the initial centrifugation at 14 000 RPM. The corresponding precipitate is P_{A14k}.

2.3.7 SN_{B1k}. Supernatant after redispersing P_{A14k} and re-centrifuging at low speed (1000 RPM). Precipitate: P_{B1k}.

2.3.8 SN_{B12k}. Supernatant after redispersing P_{A14k} and re-centrifuging at higher speed (12 000 RPM). Precipitate: P_{B12k}.

2.3.9 SN_{C1k}. Supernatant after redispersing P_{B1k} and re-centrifuging (1000 RPM).

2.3.10 SN_{C12k}. Supernatant after redispersing P_{B12k} and re-centrifuging (12 000 RPM).

3. Results and discussion

We prepared a total of five samples corresponding to different purification stages and centrifugation speeds (Scheme 1), and

Table 1 Composition of each fraction and supporting experimental evidence

Stage	Fraction	Main component	$CsPbCl_3$	Component $CsPbCl_3:Eu^{3+}$	OA + OAm + Eu^{3+} complexes
Stage A	SN_{A14k}	OA + OAm + Eu^{3+} complexes	— —	— —	Fig. 2(a) (Fig. 3(a) and 4(a))
Stage B	SN_{B1k}	OA + OAm + Eu^{3+} complexes	Fig. 1(a–c), 4(b) and Fig. S8 (Fig. 2(c))	Fig. 1(a–c), 4(a) and Fig. S8, Table S1:	Fig. 1(a and d) (Fig. 3a)
	SN_{B12k}	OA + OAm + Eu^{3+} complexes	Fig. S6(a) and S9 (Fig. 1(d))	Fig. S6(a) and Fig. 4(c and d)	Fig. 2(b) (Fig. 3(a))
Stage C	SN_{C1k}	$CsPbCl_3$	Fig. 2(c) and 4(f) (Fig. S2(d))	Fig. 4(e) (Fig. 4(a))	— —
	SN_{C12k}	$CsPbCl_3$	Fig. 2(d) and 4(h) (Fig. S2(e))	Fig. 4(g) (Fig. 4(c and d))	— —

The "main component" is assigned based on the dominant luminescent contribution within each fraction. Top rows indicate primary evidence (direct observation in the data). Bottom rows in parentheses indicate secondary evidence (assignments deduced from comparison with other measurements). A dash indicates that the component was not observed.

This journal is © the Owner Societies 2026

*Phys. Chem. Chem. Phys.*, 2026, **28**, 7191–7200 | 7193

their compositions and supporting evidence are summarized in Table 1. Stage A used the maximum speed of our centrifuge (14 000 RPM; 16 500 RCF for our rotor) to pellet as much particulate material as possible and to facilitate removal of a supernatant enriched in molecular/ligand species. Stages B and C then used two widely separated speeds—1000 RPM (80 RCF) and 12 000 RPM (11 700 RCF)—to create a strong sedimentation contrast for differential fractionation. We report both RPM and RCF because RCF is the physically relevant quantity but many prior reports provide only RPM, which depends on rotor radius. The 1000 RPM condition was chosen as the lowest speed that still produced a clean, collectable pellet/supernatant boundary, whereas 12 000 RPM reflects a commonly used upper-end condition. Under this design, the Stage B supernatant at 1000 RPM (SN_{B1k}) is expected to retain the largest overall population of dispersible nanocrystals, while the Stage B supernatant at 12 000 RPM (SN_{B12k}) should be comparatively enriched in the smallest/most dispersible species. The Stage C supernatants (SN_{C1k} and SN_{C12k}) represent the residual components that remain dispersible in toluene after further processing. The following sections describe the structural and spectroscopic characterization that underpins these assignments; deviations from the expected fractionation behavior are discussed as mechanistically informative rather than treated as experimental noise.

3.1 Reproduction of CsPbCl$_3$:Eu^{3+} and their properties

According to the previous report,[37] the target sample is the supernatant after second centrifugation (Stage B). In order to extract as many target CsPbCl$_3$:Eu^{3+} nanocrystals as possible, the speed of the second centrifugation was set to 1000 RPM (80 RCF). The obtained sample will be denoted SN_{B1k}. The

absorption and emission spectrum (369 nm excitation) of SN_{B1k} recorded 1 day after synthesis are shown in Fig. 1(a). The absorption spectrum is a featureless rise in absorbance toward shorter wavelengths, beginning below $\sim$500 nm (named Type-A1). The absence of any defined absorption peak (in contrast to the $\sim$400 nm band-edge seen in typical CsPbCl$_3$ nanocrystals, *i.e.* Type-A2 in Fig. S2(b)) suggests that the absorption of SN_{B1k} is dominated by species other than CsPbCl$_3$ nanocrystals. Meanwhile, the emission spectrum consisted of three distinct components: Type-E1, a broad band from 400–600 nm peaking near $\sim$450 nm; Type-E2, the relatively sharp excitonic emission of CsPbCl$_3$ near $\sim$405 nm;[39] and Type-E3, Eu^{3+} lines with a peak at 615 nm (parity-forbidden 4f–4f transitions: $^5D_0 \rightarrow\ ^7F_2$).[40] Consequently, the presence of Eu^{3+} line emission in an ensemble spectrum establishes that Eu^{3+} is being sensitized, but it does not uniquely identify the sensitizing species. Both lattice-incorporated Eu^{3+} and Eu-containing molecular byproducts can, in principle, produce similar Eu^{3+} emission signatures.[41,42] Previous reports on CsPbCl$_3$:Eu^{3+} nanocrystals report Type-E3 spectrum (Eu^{3+} emission) along with Type-E1 or Type-E2 spectra,[15,18,35–38,43–46] so we were able to reproduce most of the spectral features reported for these systems. We note that the Type-E3 spectrum was weak compared to the other peaks, also in alignment with the synthetic protocol we followed for this study.[37]

The temporal evolution in Fig. S3(b) further supports that the emission components originate from different species. Specifically, Type-E2 becomes undetectable after 11 days, while the other emission components remain largely unchanged. If all features arose from a single emitter population, their relative contributions would be expected to change in a correlated manner; instead, the selective disappearance of Type-E2
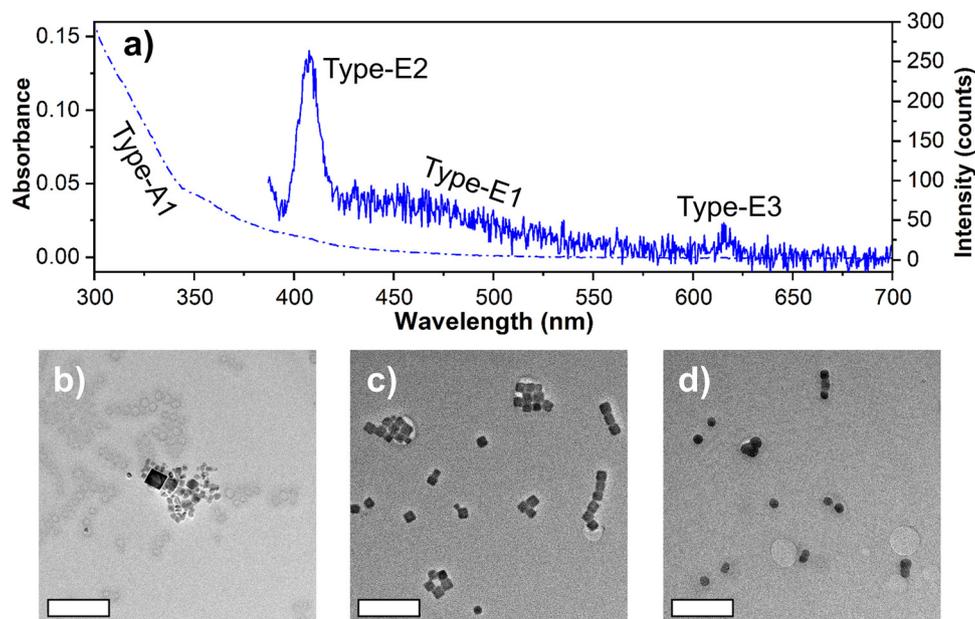
Fig. 1 Reproduced properties of CsPbCl$_3$:Eu^{3+} nanocrystals SN$_{b1k}$. (a) Ensemble absorption and emission spectrum (excitation at 369 nm) in toluene. The absorption spectrum was featureless (Type-A1). Three distinct emission bands were observed, namely broad band peaking at 450 nm (Type-E1), sharp band at 405 nm (Type-E2) from CsPbCl$_3$ nanocrystal host emission, and sharp band at 615 nm (Type-E3) characteristic of Eu^{3+} emission. (b)–(d) TEM images of the nanocrystals. Cubic nanocrystals (b) and (c) and spherical nanoparticles (d) were present. scale bars: 200 nm.

supports decoupled emission origins. This also highlights that the mere coexistence of Eu^{3+} emission and $CsPbCl_3$-related emission in an ensemble spectrum (*e.g.*, on day 1 after synthesis) is not sufficient to conclude host-sensitized Eu^{3+} emission, because distinct emissive species can contribute simultaneously to the same ensemble measurement. Further experimental evidence and discussion will be described in Section 3.2. Low emission intensity of Type-E2 spectrum in SN_{B1k} in comparison to the undoped samples (Fig. S2(b)) indicates either inefficient nanocrystal emission or low nanocrystal population, especially considering that the centrifugation speed was set low to collect as many nanoparticles as possible. Based on the absorption spectrum (which showed Type-A1), a large population of weakly emissive nanocrystals is unlikely; their strong absorption would remain visible.[47] We therefore conclude that only a small quantity of nanocrystals was present in SN_{B1k}.

We also obtained transmission electron microscope (TEM) images of SN_{B1k} (Fig. 1(b–d)). Cubic nanocrystals ($\sim$25–35 nm, Fig. 1(b and c)) and medium-sized spherical nanoparticles ($\sim$20 nm, Fig. 1(d)) were found. Zoomed-in TEM images of these particles are provided in Fig. S4(a–c). As a reference, Fig. S4(d and e) shows the undoped $CsPbCl_3$ nanocrystals under the same purification procedure, where only $\sim$7 nm cubes were observed. Based on prior reports[18–20,26–29,31] and our undoped control, the cubic nanocrystals are the target $CsPbCl_3$:Eu^{3+} material, with the remaining particles attributed to byproducts. Furthermore, energy dispersive X-ray spectroscopy (EDS) was performed on a single cubic nanocrystal and surrounding regions (Fig. S5 and Table S1). All expected elements of $CsPbCl_3$:Eu^{3+}—Cs, Pb, Cl, and Eu—were detected, indicating that the cubic $CsPbCl_3$ nanocrystals indeed contained Eu^{3+} ions. A high carbon signal was also observed at the nanocrystal location, which cannot be fully attributed to the carbon support film of the TEM grid and likely originates from surface ligands (OA/OAm), consistent with standard colloidal syntheses. In contrast, surrounding areas without visible particles showed high carbon but no detectable Eu, suggesting free ligands or organic byproducts. Overall, we were able to reproduce most properties reported previously.

3.2 Comparison with other samples and attribution of the emission types

In order to separate the emission spectral components in the mixture of the product, we also measured the absorption and emission spectrum of the sample in Stage B at 12 000 RPM (16 500 RCF). The sample will be denoted SN_{B12k}. The absorption spectrum of SN_{B12k} was identical (Type-A1) to that of SN_{B1k} (both showed Type-A1 absorption), whereas the emission lacked Type-E2 spectrum (Fig. 2(b)). This is likely because of the higher centrifugation speed that removes more $CsPbCl_3$ nanocrystals from the supernatant, thus removing most host emission. It should be noted, however, that TEM images still showed that the cubic nanocrystals (Fig. S6(a)) and medium-sized spherical nanoparticle (Fig. S6(b)) were still present in the sample, and also included large spherical nanoparticles ($\sim$40 nm, Fig. S6(c)), and small spherical nanoparticles ($\sim$5 nm, Fig. S6(d)) in addition to those observed in SN_{B1k}. The lack of Type-E2 spectrum

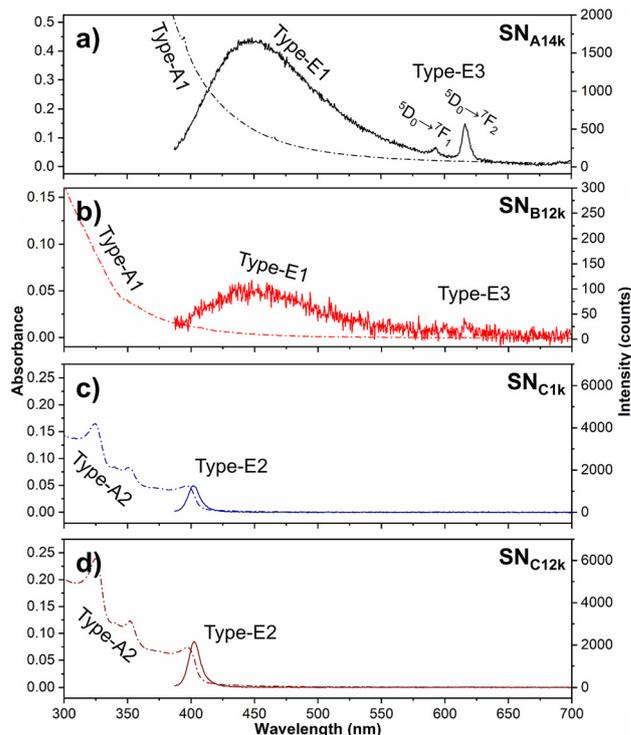**Fig. 2** Ensemble absorption and emission spectra (excitation at 369 nm) of (a) SN_{a14k}, (b) SN_{b12k}, (c) SN_{c1k}, and (d) SN_{c12k}. The absorption type (Type-A1, 2) and emission type (Type-E1–3) are indicated. The emission intensities can be qualitatively compared between the samples here and with that in Fig. 1(a) since the measurements were under the same setup.

without a major difference in the Type-E3 emission intensity indicates that $CsPbCl_3$ nanocrystal host emission and Eu^{3+} emission are not necessarily correlated at ensemble level.

Further centrifugation (Stage C) yielded samples (SN_{C1k} and SN_{C12k}) with absorption and emission spectra typically observed in $CsPbCl_3$ nanocrystals, namely Type-A1 absorption and Type-E2 emission (Fig. 2(c and d)). Minor or pronounced onsets in the absorption indicate the presence of smaller nanocrystals. The undoped control samples showed similar spectra (Fig. S2(d and e)). The centrifugation speed did not have a significant impact on the absorption and emission spectra or their intensity. Type-E1 or -E3 emission were not observed, which suggests that the nanocrystals may not exhibit any substantial Eu^{3+} emission. This raises two possibilities: Eu^{3+} ions were not incorporated into most nanocrystals, and/or Eu^{3+} ions are not emissive in this host. We further investigate these two possibilities in Section 3.3.

We also measured the absorption and emission spectra of the sample at Stage A (SN_{A14k}, Fig. 2(a)), which would provide insight into the components at the upstream of the purification process. Here, we observed Type-A1 absorption, and Type-E1 and -E3 emission. No Type-E2 emission ($CsPbCl_3$ nanocrystal host emission) was observed, implying low content of $CsPbCl_3$ nanocrystals. We note that the intensity ratio between Type-E1 and -E3 among SN_{A14k}, SN_{B1k} and SN_{B12k} is roughly similar at 3:1, suggesting that these samples share a common origin as

This journal is © the Owner Societies 2026

Phys. Chem. Chem. Phys., 2026, **28**, 7191–7200 | **7195**

well. Our spectrometer has sufficient spectral resolution to resolve Stark splitting of Eu^{3+} transitions (see Section 2.2 apparatus and Fig. S7), where the maximum number of Stark lines is $2J + 1$ and their relative intensities depend on the crystal field. If emission occurs from Eu^{3+} ions doped in the Pb^{2+} sites of $CsPbCl_3$ nanocrystals, then a well-resolved Stark splitting intrinsic to the crystal field of the Pb^{2+} site should be observed. Thus, $^5D_0 \rightarrow {}^7F_1$ ($\approx$ 584 nm) can split into up to 3 lines and $^5D_0 \rightarrow {}^7F_2$ into up to 5 lines. No splitting was observed; instead, the lines were broadened into smooth peaks, indicating a distribution of crystal-field environments (*i.e.* no single, discrete Eu^{3+} site).

We initially hypothesized that emission spectroscopy with high wavelength resolution could provide a simple, reliable check for impurities and byproducts (or their absence). If Eu^{3+} ions are successfully doped into Pb^{2+} sites in the nanocrystals without impurities, then well-resolved Stark splitting should be observed. However, a theoretical study suggested that Eu^{3+} emission in $CsPbCl_3$ nanocrystals may arise from oxygen-related surface defects, which implies that emission occurs mainly at the surface of the nanocrystals.[48] There is also some experimental evidence that suggests Ln^{3+} ions are primarily doped near the surface.[18] Because surface defects tend to be structurally heterogeneous, Eu^{3+} ions would not experience a single crystal-field environment, leading to broadened, featureless 4f-transition lines. Therefore, the spectral features (or lack thereof) are not necessarily a reliable indicator for the absence of impurities.

To identify the source of Type-E3 emission, we prepared mixtures of OA, OAm, and $Eu(NO_3)_3$ in ODE without any Cs or Pb precursors and measured their spectra (Fig. 3). $Eu(NO_3)_3$ did not dissolve in ODE by itself and was therefore unmeasurable. OAm + Eu yielded a strongly scattering dispersion with artificially high apparent absorbance (Fig. S8), so its relative emission intensity is unreliable. Type-E3 (Eu^{3+}) emission was observed for OA + Eu and OA + OAm + Eu, suggesting that Eu^{3+} emission mainly arises from OA-bound Eu^{3+} complexes. The lack of Stark resolution indicates that these species are also microheterogeneous. The integrated intensity ratio $I_{01}:I_{02}$ (emission from $^5D_0 \rightarrow {}^7F_1$ *versus* $^5D_0 \rightarrow {}^7F_2$) depends on the crystal-field symmetry[49] and can be used to compare the complexes with the doped samples. After baseline subtraction of the Type-E1 emission, the ratios were $\sim$1:7.1 for SN_{A14k} and $\sim$1:6.6 for OA + OAm + Eu mixture, possibly suggesting a common origin. And as previously mentioned, the spectral similarities between SN_{A14k}, SN_{B1k} and SN_{B12k} further suggests that SN_{B1k} and SN_{B12k} also share a common origin with OA + OAm + Eu mixture.

Type-E1 broad emission was observed in the OAm + Eu and OA + OAm + Eu mixtures as well. Notably, the peak wavelength of this emission shifted depending on the reactant combination: $\sim$415 nm for OA alone, $\sim$425 nm for OAm alone; adding $Eu(NO_3)_3$ causes a red-shift to $\sim$430 nm (for OA + Eu) and $\sim$440 nm (for OA + OAm). Three conclusions follow. First, relative to the ligands alone, $Eu(NO_3)_3$ tends to redshift the spectra, indicating chemical interaction between Eu^{3+} and the ligands. Second, because Type-E3 appears only when OA and Eu salt are both present, Eu^{3+} emission is likely photosensitized by chemically bound OA. Indeed, previous report on Eu-oleate
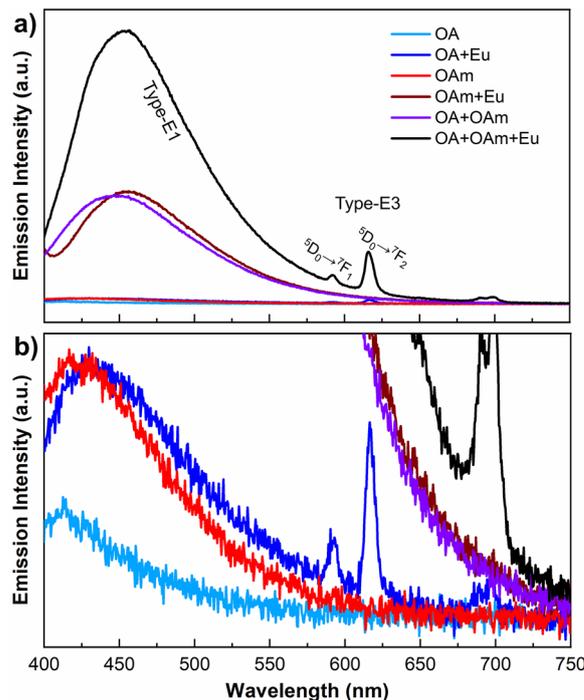

Fig. 3 (a) Ensemble emission spectra (excitation at 369 nm) of reactant combination mixture without Pb and Cs source. The emission type (Type-E1, 3) is indicated. (b) Zoomed spectra of (a) showing intensities of weakly emitting mixtures. $Eu(NO_3)_3$ is denoted simply as "Eu" for clarity.

showed that they are emissive.[50] We note that our system differs in regards to the solvent used (ODE) to synthesize them as well as the presence of OAm, which may have added the microheterogeneity owing to their long alkyl chain. Third, OA and OAm interact chemically, producing a much higher emission intensity than either ligand alone. OA and OAm are known to form an ammonium-oleate, and OAm is known to assist OA binding to perovskite surfaces.[51,52] Note: a broad blue emission (Type-E1) is also observed in undoped $CsPbCl_3$ samples in Stage-A (Fig. S2(a)), likely due to emissive ligand-related species, consistent with the emissions from OA + OAm. Thus, the spectral changes observed are consistent with these known interactions. We infer that OA + OAm + Eu forms an Eu-complex that reproduces the SN_{A14k}, SN_{B1k}, and SN_{B12k} emission spectra (neglecting host emission), suggesting that Eu^{3+} emission likely originates from this complex rather than from $CsPbCl_3$ host sensitization. The OA/OAm ligand environment is inherent to the colloidal synthesis and that any Eu not incorporated into the lattice would naturally remain as such complexes in solution. This interpretation may also explain the lower nanocrystal yield compared with undoped syntheses: the doped SN_{A14k} samples showed Type-A1 absorption, whereas undoped SN_{A14k} showed Type-A2 (Fig. S2(a)). Formation of Eu^{3+} complexes may inhibit $CsPbCl_3$ nanocrystal formation by sequestering ligands during synthesis.

3.3 Photophysical properties at single-particle level

Ensemble data on $CsPbCl_3$:Eu^{3+} suggested that Eu^{3+} emission mainly arises from complexes. However, this does not automatically

7196 | *Phys. Chem. Chem. Phys.*, 2026, **28**, 7191–7200

This journal is © the Owner Societies 2026

exclude the possibility of Eu^{3+} emission *via* $CsPbCl_3$ host sensitization, nor does it address whether Eu^{3+} is actually doped into the host. As noted in the Introduction, Ln^{3+} complexes have intrinsically long emission lifetimes (hundreds of μs to ms) compared to typical emitters like perovskite nanocrystals (few to tens of ns), so under continuous excitation emission per unit time (photon flux) in Ln^{3+} complexes is far lower than that of nanocrystal exciton emitters. In a mixture of Eu^{3+} complexes and $CsPbCl_3:Eu^{3+}$ nanocrystals, fluorescence microscopy will largely eliminate signals from complexes while directly detecting any emissive $CsPbCl_3:Eu^{3+}$ nanocrystals that are present. This means that single-particle fluorescence provides both spatial isolation of emitters and selective sensitivity to fast emitters (nanocrystals) over slow emitters (complexes).

Representative wide-field images and spectra for doped samples in Stage B (SN_{B1k} and SN_{B12k}) and C (SN_{C1k} and SN_{C12k}) are shown in Fig. 4. Samples were dispersed in 2 wt% PMMA films at the same concentration used for solution spectra and excited at 360 nm. Particles were very dilute in SN_{B1k} and SN_{B12k}; often only one particle—or none—was observed per field of view, consistent with the ensemble results. Overall, Eu^{3+} emission (Type-E3) was not observed, and particles appeared either as large, blurred (non-circular) spots or as diffraction-limited points. The majority of particles showed Type-E2 (host) emission (see Fig. S9–S12 for more examples), even for SN_{B12k} samples where host emission was undetectable at the ensemble level. The appearance of Type-E2 at the single-particle level but not in ensemble spectra likely reflects the very low number of emitting nanocrystals, which kept the ensemble signal below the detection threshold. Conversely, the ensemble Type-E1 band likely arises from a weakly emissive but abundant species—consistent with the OA/OAm salt and Eu^{3+} complexes.

Many particles also showed a broad and featureless anomalous band from 500–650 nm peaking inhomogeneously at 580–590 nm (Type-E4), irrespective of the observed particle size. Type-E4 signals were generally weak (low S/N) and were accompanied by relatively weak Type-E2 emission (*e.g.*, Fig. 4(a, c, e and g)). In contrast, particles without Type-E4 exhibited intense, high-S/N Type-E2 emission (*e.g.*, Fig. 4(b, d, f and h)). Type-E4 was not observed for undoped $CsPbCl_3$, implying that it is exclusive to doped samples. The fraction of particles exhibiting Type-E4 emission was not markedly different from that of particles without Type-E4; however, because Type-E4 is very weak while Type-E2 is substantially stronger, the Type-E4 component is likely averaged out or buried below the noise floor in ensemble measurements. This observation underscores the utility of single-particle fluorescence microscopy for resolving emissive components that are rare and/or weak yet spatially localized. Three attributions are possible for Type-E4: (1) defect emission[28,35] (especially under charge imbalance from Ln^{3+} incorporation[35]), (2) a defect-assisted charge-transfer state (CTS, a dopant-centered charge-transfer state, see below),[44,46] and (3) Eu^{2+} emission.[53,54] Eu^{2+} 4f–5d emission in chloride perovskites occurs at much higher energy (bluer) than 580–590 nm; thus, the Eu^{2+} assignment is less consistent with our observed band position.[54] All three scenarios, however, require the presence of Eu in or near the lattice, which—along with the EDS evidence of Eu—indicates that Type-E4 is a consequence of successful Eu incorporation. Furthermore, Type-E1 and Type-E4 are distinct broad emissions: E1 originates from abundant ligand-bound species (appearing in ensemble spectra), whereas E4 is an entirely different, dopant-associated emission that is only discernible at the single-particle level.

Irrespective of whether Type-E4 arises from a defect state or a CTS, the presence of an intermediate level near 580–590 nm
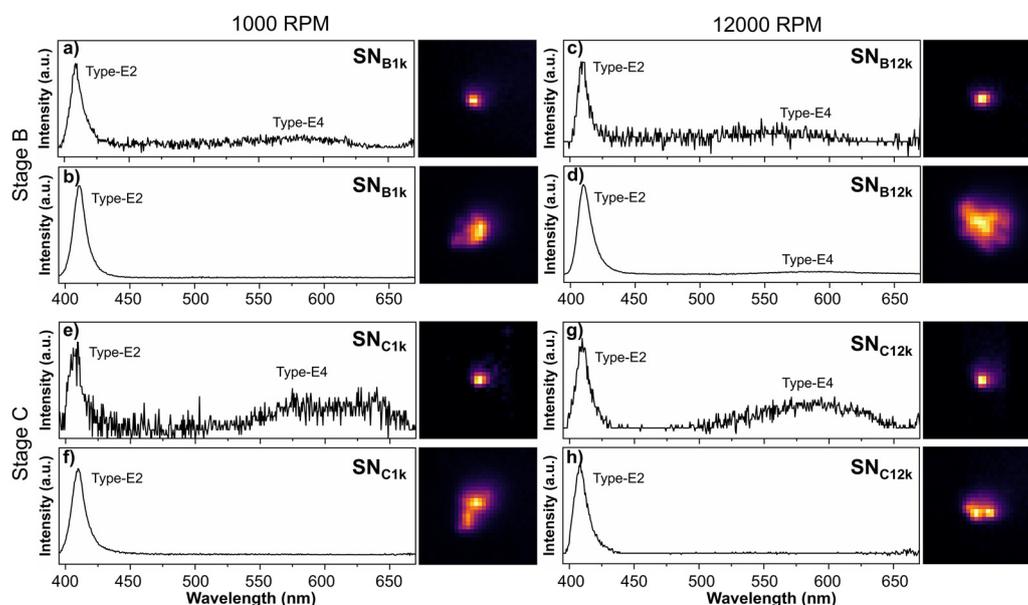

Fig. 4 Representative fluorescence microscope images (excitation at 360 nm) of the particles and their emission spectra. (a) and (b) SN_{b1k}, and (c) and (d) SN_{b12k}. (e) and (f) SN_{c1k}, and (g) and (h) SN_{c12k}. All images are 4.8 μm × 4.8 μm. Panels (a), (c), (e) and (g) show particles exhibiting the weak broad emission, Type-E4; panels (b), (d), (f) and (h) show particles with mainly strong excitonic emission, Type-E2.

($\sim$17 000 cm^{-1}) suggests that host-sensitized Eu^{3+} emission is disfavored because the Eu^{3+} emitting level $^5D_0$ lies at a comparable energy.[40] Population reaching $^5D_0$ can undergo rapid nonradiative relaxation (e.g., back-transfer) via this intermediate rather than yield Eu^{3+} 4f–4f emission.

Under the defect-assisted sensitization model proposed for Yb-doped CsPbCl$_3$ (Fig. 5(a)), the photophysical pathway involves a host-derived defect state feeding a lanthanide-centered charge-transfer state (CTS), i.e. [Ln^{3+}–Cl$^-$–V$_{Pb}^{2-}$–Cl$^-$–Ln^{3+}]$^-$ to [Ln^{2+}–Cl$^-$–V$_{Pb}^{2-}$–Cl$^-$–Ln^{3+}], which then populates the dopant's 4f excited manifold.[44,46] A key consequence is that the defect level is primarily host-derived, whereas the CTS energy is dopant-dependent (through local structure and the fixed relationship between lanthanides in Ln^{3+}/Ln^{2+} redox potentials[55,56]). A Yb-centered CTS is expected at higher energy than the Eu-centered CTS by approximately 6450 cm^{-1}.[55,56] If we were to assign Type-E4 emission to defect emission, then (because the defect is host-set) the Eu-centered CTS would have to lie far below $\sim$17 000 cm^{-1}, i.e., in the near-IR, which has not been reported for any host material up to date. Conversely, assigning the 580–590 nm band to the CTS (which is Eu-linked and therefore dopant-dependent) resolves this conflict. We therefore favor a CTS assignment for Type-E4 emission, which is in agreement with the previous report.[41] As illustrated in Fig. 5(b), after the excitation of the CsPbCl$_3$ nanocrystal host, the relaxation process is a charge separation into clustered host-derived defect state (state (1)), and then a relaxation to the CTS state (state (2)) directly or through the $^5D_0$ state of Eu^{3+} ion (state (3)). Emitter state of Eu^{3+} ions ($^5D_0$ level) lies at $\sim$17 300 cm^{-1}—comparable to the CTS state—and cannot be efficiently populated. Taken together, this analysis underscores why Yb^{3+} remains viable in CsPbCl$_3$: the Yb^{3+} 4f excited manifold ($^2F_{5/2}$, $\sim$10 200 cm^{-1}) lies well below the intermediate, which suppresses back-transfer and agrees with reports of host-sensitized Yb^{3+} emission in CsPbCl$_3$.[16,18,44,57–64]

These considerations also point to an engineering route: if the CTS corresponds to a dopant-vacancy cluster (e.g. [Ln^{3+}–Cl$^-$–V$_{Pb}^{2-}$–Cl$^-$–Ln^{3+}]$^-$ to [Ln^{2+}–Cl$^-$–V$_{Pb}^{2-}$–Cl$^-$–Ln^{3+}] transition[44,57]), then strategies that reduce deep vacancy formation and strengthen halide passivation (i.e., using X-type, Cl-donating ligands)[65] could destabilize energy or decouple the CTS, potentially making Eu^{3+} emission more favorable. Overall, lanthanide emission in CsPbCl$_3$ cannot be rationalized by simple energy-gap matching alone; one must account for the existence, energy, and coupling of intermediate states and assess their compatibility with the lanthanide in question.

We cannot determine whether the absence of Eu^{3+} f–f lines is due to insufficient dopant concentration (below our detection threshold) or an intrinsic inability of CsPbCl$_3$:Eu^{3+} to sensitize Eu^{3+} under the mechanism described above. Furthermore, our results pertain to the specific synthetic method we employed; minor to major differences may be present in other systems. Indeed, across reports on CsPbCl$_3$:Eu^{3+} nanocrystals, one or more of Type-E1, -E2, and -E3 are often missing.[15,18,35–38] Consequently, Eu^{3+} emission requires careful assignment—particularly at the ensemble level—before attributing it to host-sensitized dopants. Reliable ensemble measurements further require verified purification, because impurities and by-products generated during synthesis can obscure the true emission origin.

4. Conclusions

We investigated ensemble and single-particle emission from Eu-treated CsPbCl$_3$ nanocrystals purified at different centrifugation speeds. The main points are:

• Conventional hot-injection synthesis of CsPbCl$_3$:Eu^{3+} yields mixed NCs and molecular/inorganic species; Stage-A

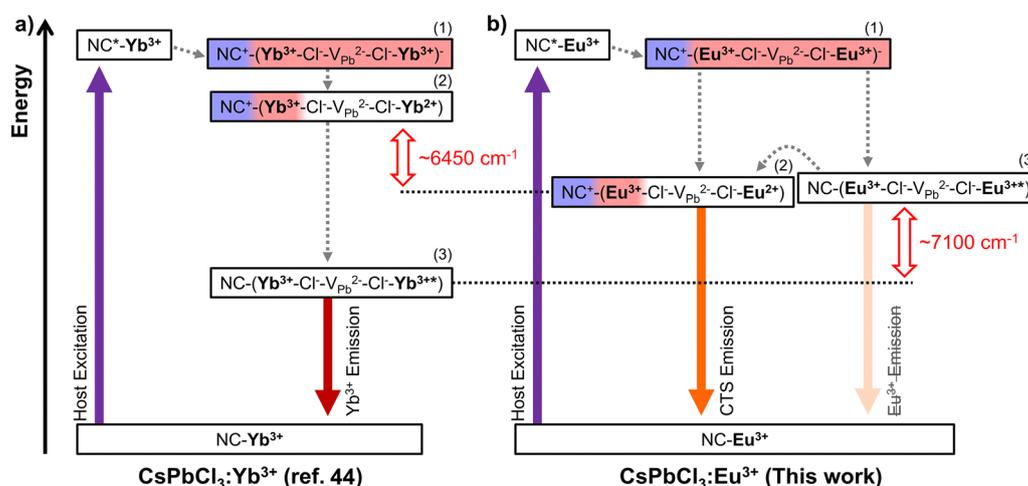Fig. 5 Energy diagram of (a) CsPbCl$_3$:Yb^{3+} (based on the report by W. Chang et al.[44]), and (b) CsPbCl$_3$:Eu^{3+} in this work. The star represents neutrally excited state. The color on the states represents positive charge (blue) and negative charge (red) and their degree of localization. State (1) is a clustered host-derived defect state, state (2) is the CTS, and state (3) is the localized 4f-excited state of the lanthanide. The energy difference between state (2) of CsPbCl$_3$:Yb^{3+} and CsPbCl$_3$CsPbCl$_3$:Eu^{3+} is based on the ln^{3+}/ln^{2+} redox potential and is practically fixed at $\sim$6450^{-1} under the same host. The energy difference between state (3) of the two compounds are intrinsically fixed at $\sim$7100^{-1} regardless of the host material.

7198 | Phys. Chem. Chem. Phys., 2026, 28, 7191–7200

This journal is © the Owner Societies 2026

centrifugation at 14 000 RPM (16 500 RCF) should partition them, yet the supernatant fractions of the Stage-B centrifugation (SN_{B1k} and SN_{B12k}) that are often used in prior reports continued to exhibit molecular-origin emission.

• In ensemble spectra, the dominant source of Eu^{3+} lines was microheterogeneous Eu–ligand complexes formed with OA/OAm (as evidenced by Eu^{3+} emission in OA/OAm + Eu salt without Cs/Pb).

• Eu^{3+} ions may be incorporated into the $CsPbCl_3$ host, but an additional broad 500–650 nm band appears (Type-E4) with no accompanying Eu^{3+} lines, even from individual particles.

• The weak band near 580–590 nm ($\sim 17\,000$ cm^{-1}) is most consistently interpreted as a dopant-linked intermediate (defect-assisted CTS) lying close to the Eu^{3+} $^5D_0$ energy and therefore in a strong competition with Eu^{3+} f–f emission *via* back-transfer.

We emphasize the distinction between successful doping and dopant-origin emission under typical syntheses. Reliable attribution requires verified purification and corroborating single-particle data—ensemble Eu^{3+} lines alone are insufficient when Eu–ligand complexes and intermediate states may contribute because both lattice-incorporated Eu^{3+} and Eu-complex byproducts can produce similar Eu^{3+} emission lines. More broadly, band-gap alignment by itself is inadequate; one must also evaluate whether defect/CTS intermediates exist, where they lie energetically, and how strongly they couple to the lanthanide levels. Adopting such stringent criteria will sharpen the basis on which lanthanide emission is assigned in perovskite nanocrystal studies going forward.

Author contributions

S. O. and M. V. contributed to the conceptualization of the study. S. O. contributed to the design of the experiments and wrote the manuscript. S. O. and mainly Y. W. contributed to the synthesis, materials measurements, and data analysis. S. O., Y. W., and M. V. contributed to the discussion of the data. All authors contributed to the manuscript revision and read and approved the submitted version.

Conflicts of interest

There are no conflicts to declare.

Data availability

The data supporting this article have been included as part of the supplementary information (SI). Supplementary information: Single-particle spectroscopy setup (Fig. S1). Ensemble absorption and emission spectra of non-doped $CsPbCl_3$ nanocrystal samples (Fig. S2). Ensemble absorption and emission spectra of $CsPbCl_3$:Eu^{3+} nanocrystal samples 11 days after synthesis (Fig. S3). Zoomed images of TEM images of SN_{B1k} (Fig. S4). Spot selected for EDS measurements (Fig. S5). EDS results (Table S1). TEM images of SN_{B12k} (Fig. S6). Emission spectra of a fluorescent lamp measured under the same fluorescence spectrometer (Fig.

S7). Ensemble absorption spectra of reactant combination mixture without Pb and Cs source (Fig. S8). More representative fluorescence microscope images of the particles (Fig. S9–S12). See DOI: https://doi.org/10.1039/d6cp00181e.

References

1 J.-C. G. Bünzli, *Coord. Chem. Rev.*, 2015, **293–294**, 19–47.
2 J. Kido and Y. Okamoto, *Chem. Rev.*, 2002, **102**, 2357–2368.
3 A. J. Amoroso and S. J. Pope, *Chem. Soc. Rev.*, 2015, **44**, 4723–4742.
4 W. Zheng, P. Huang, D. Tu, E. Ma, H. Zhu and X. Chen, *Chem. Soc. Rev.*, 2015, **44**, 1379–1415.
5 T. Jüstel, H. Nikol and C. Ronda, *Angew. Chem., Int. Ed.*, 1998, **37**, 3084–3103.
6 V. Pankratov, A. I. Popov, S. A. Chernov, A. Zharkouskaya and C. Feldmann, *Phys. Status Solidi B*, 2010, **247**, 2252–2257.
7 V. Dubey, J. Kaur and S. Agrawal, *Res. Chem. Intermed.*, 2014, **41**, 4727–4739.
8 J. C. Bünzli and C. Piguet, *Chem. Soc. Rev.*, 2005, **34**, 1048–1077.
9 A. Tew, L. van Turnhout, Y. Deng, R. Arul, J. Ye, T. Liu, Z. Jiang, L. Dai, H. Zhu, Y. Zhang, A. Rao and Z. Yu, *Appl. Phys. Rev*, 2024, **11**, 021329.
10 B. Julián, J. Planelles, E. Cordoncillo, P. Escribano, P. Aschehoug, C. Sanchez, B. Viana and F. Pellé, *J. Mater. Chem.*, 2006, **16**, 4612–4618.
11 R. Martin-Rodriguez, R. Geitenbeek and A. Meijerink, *J. Am. Chem. Soc.*, 2013, **135**, 13668–13671.
12 Z. Chen, Y. Li and L. Wu, *Nanoscale Adv.*, 2023, **5**, 1397–1404.
13 J. Planelles-Aragó, B. Julián-López, E. Cordoncillo, P. Escribano, F. Pellé, B. Viana and C. Sanchez, *J. Mater. Chem.*, 2008, **18**, 5193–5199.
14 Y. Wang, X. Liang, E. Liu, X. Hu and J. Fan, *Nanotechnol.*, 2015, **26**, 375601.
15 Q. Li, Y. Liu, P. Chen, J. Hou, Y. Sun, G. Zhao, N. Zhang, J. Zou, J. Xu, Y. Fang and N. Dai, *J. Phys. Chem. C*, 2018, **122**, 29044–29050.
16 T. J. Milstein, D. M. Kroupa and D. R. Gamelin, *Nano Lett.*, 2018, **18**, 3792–3799.
17 R. Sun, P. Lu, D. Zhou, W. Xu, N. Ding, H. Shao, Y. Zhang, D. Li, N. Wang, X. Zhuang, B. Dong, X. Bai and H. Song, *ACS Energy Lett.*, 2020, **5**, 2131–2139.
18 G. Pan, X. Bai, D. Yang, X. Chen, P. Jing, S. Qu, L. Zhang, D. Zhou, J. Zhu, W. Xu, B. Dong and H. Song, *Nano Lett.*, 2017, **17**, 8005–8011.

This journal is © the Owner Societies 2026

Phys. Chem. Chem. Phys., 2026, **28**, 7191–7200 | 7199

19 D. Zhou, D. Liu, G. Pan, X. Chen, D. Li, W. Xu, X. Bai and H. Song, *Adv. Mater.*, 2017, **29**, 1704149.

20 J. Duan, Y. Zhao, X. Yang, Y. Wang, B. He and Q. Tang, *Adv. Energy Mater.*, 2018, **8**, 1802346.

21 X. Zhang, Q. Zhu, B. Chen, S. Wang, A. L. Rogach and F. Wang, *Adv. Photonics Res.*, 2020, **2**, 2000089.

22 Q. Xiao, Y. Liu, L. Liu, R. Li, W. Luo and X. Chen, *J. Phys. Chem. C*, 2010, **114**, 9314–9321.

23 J. Kong, H. Zhu, R. Li, W. Luo and X. Chen, *Opt. Lett.*, 2009, **34**, 1873–1875.

24 H. Zhang, Z.-H. Chen, X. Liu and F. Zhang, *Nano Res.*, 2020, **13**, 1795–1809.

25 G. H. Debnath, P. Mukherjee and D. H. Waldeck, *J. Phys. Chem. C*, 2020, **124**, 26495–26517.

26 R. Marin and D. Jaque, *Chem. Rev.*, 2021, **121**, 1425–1462.

27 Y. Xie, B. Peng, I. Bravic, Y. Yu, Y. Dong, R. Liang, Q. Ou, B. Monserrat and S. Zhang, *Adv. Sci.*, 2020, **7**, 2001698.

28 J. Y. D. Roh, M. D. Smith, M. J. Crane, D. Biner, T. J. Milstein, K. W. Krämer and D. R. Gamelin, *Phys. Rev. Mater.*, 2020, **4**, 105405.

29 J.-P. Ma, Y.-M. Chen, L.-M. Zhang, S.-Q. Guo, J.-D. Liu, H. Li, B.-J. Ye, Z.-Y. Li, Y. Zhou, B.-B. Zhang, O. M. Bakr, J.-Y. Zhang and H.-T. Sun, *J. Mater. Chem. C*, 2019, **7**, 3037–3048.

30 W. J. Mir, T. Sheikh, H. Arfin, Z. Xia and A. Nag, *NPG Asia Mater.*, 2020, **12**, 9.

31 W. Xu, J. Liu, B. Dong, J. Huang, H. Shi, X. Xue and M. Liu, *Sci. Adv.*, 2023, **9**, eadi7931.

32 D. J. Gargas, E. M. Chan, A. D. Ostrowski, S. Aloni, M. V. Altoe, E. S. Barnard, B. Sanii, J. J. Urban, D. J. Milliron, B. E. Cohen and P. J. Schuck, *Nat. Nanotechnol.*, 2014, **9**, 300–305.

33 A. D. Ostrowski, E. M. Chan, D. J. Gargas, E. M. Katz, G. Han, P. J. Schuck, D. J. Milliron and B. E. Cohen, *ACS Nano*, 2012, **6**, 2686–2692.

34 J. A. O. Galindo, A. R. Pessoa, A. M. Amaral and L. D. S. Menezes, *Nanoscale Adv.*, 2021, **3**, 6231–6241.

35 R. Sun, D. Zhou, Y. Ding, Y. Wang, Y. Wang, X. Zhuang, S. Liu, N. Ding, T. Wang, W. Xu and H. Song, *Light: Sci. Appl.*, 2022, **11**, 340.

36 X. Jing, D. Zhou, R. Sun, Y. Zhang, Y. Li, X. Li, Q. Li, H. Song and B. Liu, *Adv. Funct. Mater.*, 2021, **31**, 2100930.

37 W. Wang, S. Song, P. Lv, J. Li, B. Cao and Z. Liu, *J. Lumin.*, 2023, **260**, 119894.

38 G. H. Debnath, B. P. Bloom, S. Tan and D. H. Waldeck, *Nanoscale*, 2022, **14**, 6037–6051.

39 L. Protesescu, S. Yakunin, M. I. Bodnarchuk, F. Krieg, R. Caputo, C. H. Hendon, R. X. Yang, A. Walsh and M. V. Kovalenko, *Nano Lett.*, 2015, **15**, 3692–3696.

40 K. Binnemans, R. Van Deun, C. Görller-Walrand and J. L. Adam, *J. Non-Cryst. Solids*, 1998, **238**, 11–29.

41 S. Miyazaki, M. Gotanda, Y. Kitagawa, Y. Hasegawa, K. Miyata and K. Onda, *J. Phys. Chem. Lett.*, 2024, **15**, 10718–10724.

42 J. Sun, H. Fu, H. Jing, X. Hu, D. Chen, F. Li, Y. Liu, X. Qin and W. Huang, *Adv. Mater.*, 2025, **37**, e2417397.

43 Y. Liu, G. Pan, R. Wang, H. Shao, H. Wang, W. Xu, H. Cui and H. Song, *Nanoscale*, 2018, **10**, 14067–14072.

44 W. J. Chang, S. Irgen-Gioro, S. Padgaonkar, R. López-Arteaga and E. A. Weiss, *J. Phys. Chem. C*, 2021, **125**, 25634–25642.

45 W. Wang, S. Song, B. Cao and J. Li, *J. Lumin.*, 2022, **247**, 118901.

46 A. Shukla, G. Kaur, K. J. Babu, A. Kaur, D. K. Yadav and H. N. Ghosh, *J. Phys. Chem. Lett.*, 2022, **13**, 83–90.

47 S. Mannar, P. Mandal, A. Roy and R. Viswanatha, *J. Phys. Chem. Lett.*, 2022, **13**, 6290–6297.

48 A. Bala and V. Kumar, *ACS Appl. Nano Mater.*, 2020, **3**, 4437–4444.

49 P. A. Tanner, *Chem. Soc. Rev.*, 2013, **42**, 5090–5101.

50 G. Liu, C. E. Conn and C. J. Drummond, *J. Phys. Chem. B*, 2009, **113**, 15949–15959.

51 G. Almeida, L. Goldoni, Q. Akkerman, Z. Dang, A. H. Khan, S. Marras, I. Moreels and L. Manna, *ACS Nano*, 2018, **12**, 1704–1711.

52 J. De Roo, M. Ibanez, P. Geiregat, G. Nedelcu, W. Walravens, J. Maes, J. C. Martins, I. Van Driessche, M. V. Kovalenko and Z. Hens, *ACS Nano*, 2016, **10**, 2071–2081.

53 H. Yuan, S. Jin, S. Zheng, R. Xie, T. Pang, B. Zhuang, F. Huang and D. Chen, *J. Mater. Chem. C*, 2024, **12**, 1430–1439.

54 F. Alam, K. D. Wegner, S. Pouget, L. Amidani, K. Kvashnina, D. Aldakov and P. Reiss, *J. Chem. Phys.*, 2019, **151**, 231101.

55 P. Dorenbos, *J. Electrochem. Soc.*, 2005, **152**, H107.

56 P. Dorenbos, *J. Lumin.*, 2007, **122–123**, 315–317.

57 X. Li, S. Duan, H. Liu, G. Chen, Y. Luo and H. Agren, *J. Phys. Chem. Lett.*, 2019, **10**, 487–492.

58 X. Zhang, Y. Zhang, X. Zhang, W. Yin, Y. Wang, H. Wang, M. Lu, Z. Li, Z. Gu and W. W. Yu, *J. Mater. Chem. C*, 2018, **6**, 10101–10105.

59 T. Cai, J. Wang, W. Li, K. Hills-Kimball, H. Yang, Y. Nagaoka, Y. Yuan, R. Zia and O. Chen, *Adv. Sci.*, 2020, **7**, 2001317.

60 W. J. Mir, Y. Mahor, A. Lohar, M. Jagadeeswararao, S. Das, S. Mahamuni and A. Nag, *Chem. Mater.*, 2018, **30**, 8170–8178.

61 M. A. Padhiar, S. Zhang, M. Wang, N. Zamin Khan, S. Iqbal, Y. Ji, N. Muhammad, S. A. Khan and S. Pan, *Nanomaterials*, 2023, **13**, 2703.

62 X. Luo, T. Ding, X. Liu, Y. Liu and K. Wu, *Nano Lett.*, 2019, **19**, 338–341.

63 D. Li and G. Chen, *J. Phys. Chem. Lett.*, 2023, **14**, 2837–2844.

64 S. M. Loh, Y. Jing, T. C. Sum, A. Bruno, S. G. Mhaisalkar and S. A. Blundell, *J. Phys. Chem. Lett.*, 2025, **16**, 2295–2300.

65 N. C. Anderson, M. P. Hendricks, J. J. Choi and J. S. Owen, *J. Am. Chem. Soc.*, 2013, **135**, 18536–18548.

7200 | *Phys. Chem. Chem. Phys.*, 2026, **28**, 7191–7200

This journal is © the Owner Societies 2026